Engineering with Computers (2023) 39:45–59
https://doi.org/10.1007/s00366-021-01503-7

ORIGINAL ARTICLE

Strong-form meshfree collocation method for non-equilibrium solidification of multi-component alloy

Peter Schae□erkoetter[1] · John G. Michopoulos[2] · Jeong-Hoon Song[1]

Received: 29 June 2021 / Accepted: 21 August 2021 / Published online: 8 September 2021

Abstract
This work presents a strong form meshfree collocation method for a multi-phase field model with finite dissipation e ects due to rapid solidification. We use the collocation method to simulate and study solidification of a low concentration (0.2 at% Sn) Al–Sn binary alloy system under periodic boundary conditions to address non-equilibrium solidification. Numerical implementation takes place through spatial discretization of the governing equations with the collocation method followed by application of the Crank–Nicolson method to integrate through time. Analysis begins with a benchmark, a simple two-grain case with symmetry in domain size, grain positioning, and boundary conditions to study the behavior of the field equations and key terms embedded within. This occurs by studying field and embedded term values along the axis of symmetry. Solidification analysis is then extended for 10 and 20 grains where upon full solidification, the regions with the highest overall concentrations exist within grain boundary region consisting for four or more adjacent grains. An analysis of alloy solidification over a substrate demonstrates epitaxial nucleation and growth.

Keywords Multi-component alloy · Non-equilibrium · Solidification · Phase field model · Strong form · Meshfree collocation

1 Introduction

Solidification is a phase transformation process of a liquid to solid that mainly determines crystallographic characteristics of polycrystalline materials. A polycrystalline microstructure of metallic materials consists of multiple grains with di erent crystallographic orientations which are separated by grain boundaries. Such a grain structure evolves during the solidification process via grain growth. The importance of polycrystalline microstructures in being associated with many of the macroscopic mechanical properties has been well known [1–3].

Rapid solidification processes occur at extremely small timescales, leaving tgrowth patterns [20]. More recently, a multiscale coupled finite element and phase field framework for the prediction of stressed grain growth has been developed [21].

In this work, we explore the multi-phase field model of Steinbach et al. [8] with a recently developed strong form-based collocation method [22–24] to consider the rapid solidification of multi-component alloy system. In this multi-phase field model, the energy functional F comprised

✉ Jeong-Hoon Song
jh.song@colorado.edu

[1] Department of Civil, Environmental and Architectural Engineering, University of Colorado, Boulder, CO 80309, USA

[2] Computational Multiphysics Systems Laboratory, Naval Research Laboratory, Washington, DC 20375, USA

of interfacial f^{int} and chemical f^{chem} energy densities. The alloy concentration field c is split into phase concentrations c_α for each phase α; note that c_α is related to c through the weighted sum $c_\alpha \phi_\alpha$ by $c = \sum_{\alpha=1}^{N} c_\alpha \phi_\alpha$ where ϕ_α is the phase field for α. The Gibbs free energy,

$$f_{\alpha}^{c\ em} = \sum_{\gamma=1}^{N} \phi_{\gamma} f_{\gamma}(\mathbf{c}_{\gamma}) + \sum_{i=1}^{n-1} \lambda_{\alpha}^{i} \left(c_{\alpha}^{i} - \phi_{\alpha} c_{\alpha}^{i} - \phi\ c^{i} \right). \tag{17}$$

where $\sigma_{\alpha\beta}$ is the interfacial energy between phases α and $\square$, η is the interface width which is set to a constant for all interfaces in this study, and f_{γ} is the bulk free energy of phase γ. Note that the last terms in Eqs. (16) and (17), i.e. $\sum_{\gamma=1}^{N} \phi_{\gamma} = 1$ and $c_{\alpha\beta}^{i} = \phi_{\alpha} c_{\alpha}^{i} + \phi_{\beta} c_{\beta}^{i}$ implies the constraint conditions which are described in terms of Lagrange multipliers, respectively.

Derivation of the rate ϕ_{α} occurs through the first variation of the free energy functional F:

$$\frac{\partial \phi_{\alpha}}{\partial t} = \frac{\delta F(\phi_{\alpha})}{\delta \phi_{\alpha}} = \left(\nabla \frac{\partial F}{\partial \nabla \phi_{\alpha}} - \frac{\partial F}{\partial \phi_{\alpha}} \right) \tag{18}$$

The rate change of the phase field ϕ_{α} is then written as [8]:

$$\begin{aligned} \frac{}{t} &= -\frac{1}{N} \sum_{=1}^{N} \left[\frac{}{4} \left(\frac{F}{} - \frac{F}{} \right) \right] \\ &= \frac{1}{N} \sum_{=1}^{N} \frac{\psi}{t} \end{aligned} \tag{19}$$

where

$$\begin{aligned} \frac{'\ ,\beta}{'t} = K_{,\beta} \Big\{ \Big[\sigma_{,\beta} \left(I_{,} - I_{\beta} \right) \\ + \sum_{\gamma=1, \gamma\neq,\gamma\neq\beta}^{N} \left(\sigma_{\beta\gamma} - \sigma_{,\gamma} \right) I_{\gamma} \Big] + \frac{\pi^2}{4\eta} \Delta g_{,\beta} \Big\} \end{aligned} \tag{20}$$

$$I_{\gamma} = \nabla^2 \phi_{\gamma} + \frac{\pi^2}{\eta^2} \phi_{\gamma} \tag{21}$$

$$K_{\square\square} = \frac{4N\square \left(\square_{\square} + \square_{\square} \right) \square_{\square\square}}{4N\square \left(\square_{\square} + \square_{\square} \right) + \square_{\square\square}\square^2 \sum_{i=1}^{n-1} \frac{\left(c_{\square}^{i} - c_{\square}^{i} \right)^2}{p_{\square\square}^{i}}} \tag{22}$$

$$\Delta g_{\square\square} = f_{\square} - f_{\square} - \sum_{i=1}^{n-1} \frac{\square_{\square} \square_{\square}^{i} + \square_{\square} \square_{\square}^{i}}{\square_{\square} + \square_{\square}} \left(c_{\square}^{i} - c_{\square}^{i} \right) \tag{23}$$

As shown in Eq. (19) the phase field and its rate are determined by the sum total of interface fields $\frac{\square\square_{\square\square}}{\square t}$ for all active phase pairs ϕ_{α} and ϕ_{β} acting at each point in a region of active phase transformation, i.e. $0 > \phi_{\alpha} > 1$ called the *interphase region*. The evolution of each phase pair within this interfacial region as described by Eq. (20) is driven by *thermodynamic* or *chemical* source term $\Delta g_{\square\square}$. Note that the driving force $\Delta g_{\square\square}$ depends on by di erences in temperature T and phase composition c that determine Gibbs free energy $f_{\alpha}(T, c_{\alpha})$ and $f_{\square}(T, c_{\square})$, and their derivatives $\tilde{\mu}_{\alpha}^{i}$

4 Numerical examples

4.1 Non-equilibrium solidification of Al–Sn binary alloy

All examples within Sect. 4 consider solidification of Al-0.2 at% Sn alloy with FCC-A1 and BCT-A5 phases present in the system. The eutectic temperature, i.e. the FCC and BCT solidification point, occurs at 502 K. Our region of interest for this study is located within the encircled region of Fig. 1a where at 860 K the FCC phase precipitates out of solution above the eutectic temperature. The FCC and liquid Gibbs

rendering of the discretized system with two grains at the early stages of growth is shown in Fig. 2.

In this case, there exist three phase fields $\alpha \square \{1, 2, 3\}$ where 1 = liquid, 2 = grain$_1$, and 3 = grain$_2$ and each phase field is endowed with its own independent concentration, c_α, field. The concentration of Sn in Al, i.e. c^{Sn} at any point [9] is then given by:

along with the constraint condition

To examine each of the terms in Eq. (20), it is helpful to perform a visual dissection of the rate equation. This is shown in Fig. 3, which consist of a snapshot of the phase field profile at the 100th step in the simulation with corresponding section values along the centerline at $\square = (0, L/2)$. The centerline values in Fig. 3b represent the terms embedded within Eq. (20). These energy terms, one of geometry and the other chemical are generally of opposite sign and in this case, the chemical energy clearly dominates in magnitude. This results in a positive sum as shown with the dashed line in Fig. 3b, thereby driving the material towards solidification. The sum is scaled by the kinetic coe cient as described by Eq. (22) to produce the phase field rate shown in Fig. 3c, which over an increment of time, yields changes to the phase field geometry. The changing phase field geometry evolves into a shape that tends to temper or resist the chemical driving force. This is evi4(o-22)Tjm%se.1(tr)e inflg sects

Temperature is only independent parameter external to the system and it along with the phase composition, feed the chemical potential and its force gradient.

We now move to the concentration field where per Eq. (31), sum of phase weighted components $\phi_\alpha c_\alpha$ determines the overall concentration field c^{Sn}. Therefore, it is of interest to understand the e ect of $\phi_\alpha c_\alpha$ on the evolution of c^{Sn}. Our analysis begins with the concentration fields displayed in Fig. 4 at six instances in time detailing the overall concentration field and its phase weighted components. For reference a phase field surface plot is also embedded within each frame. Recall, that the phase weighted concentration profiles are initialized to 0.02 at% Sn. Regions of active phase transformation are bounded with the dashed lines of the cross-sectional plots. Evolution begins with a liquid to solid transition about the initial seed locations, Fig. 4a, b, eventually leading to small region that is fully solidified Fig. 4c, and finally radial growth Fig. 4d–f. Only the di usion term, i.e. the first term in Eq. (24) a ects the concentration rate for points outside of the interphase region where for this set of points $c^{\mathrm{Sn}}_{\mathrm{liq}} = \phi_{\mathrm{liq}} c_{\mathrm{liq}}$ and $c^{\mathrm{Sn}}_{\mathrm{sol}} = \phi_{\mathrm{sol}} c_{\mathrm{sol}}$ are constant. Concentration values for points located close to the outer edge but still within the interphase or transition region undergo an initial redu.299909ue to t9

computational requirements for temporal integration, however, appear to exhibit quadratic rate. This is attributed to the fact that finer discretizations produce more points within the interphase region.

Now consider the case of 10 grains with the same material properties as given in Table 1. Recognize that each grain is *assigned* a phase where inter-grain permeabilities and mobilities between solid/grain phases are set to zero. Ten seeds are randomly distributed throughout the domain with a uniform initialization of all concentration fields c_α at a value of 0.02 at% Sn in Al. Fig. 6 is a collection of concentration and phase values observed at six instances of time. The liquid phase concentration component $\phi_{\text{liq}} c_{\text{liq}}$ initially dominates the overall field behavior Fig. 6a. At this stage, Sn particles begin to evacuate out of the solidifying material resulting in an elevated concentration profile extending from the outer rim of the interphase region into the liquid. Driven by its gradient, the elevated concentration fields then radiate out towards and eventually join one another Fig. 6b, c. Solid–solid interphase evolution is suppressed in active regions involving two or more grains. This is attributed to the impermeability condition which drives the kinetic coe - cient $K_{\square\square}$ to zero. Grain growth partitions the liquid into distinct areas, each enclosed by an intergrain boundary, resulting in an overall increase in concentration within these areas Fig. 6d. and continues until the domain is fully solidified Fig. 6e. As shown in Fig. 6o, higher concentrations of Sn in the fully solidified material occur at the grain boundaries with the highest levels located at intergrain regions consisting of four or more adjacent grains.

4.2 Epitaxial growth

Some manufacturing and joining processes including additive manufacturing and welding involve solidifying a liquid metal over a solid substrate [3]. The solid substrate serves as a site for epitaxial nucleation whereby newly formed crystals nucleate at the adjacent substrate grains. Furthermore, the crystal's crystallographic orientation does not change throughout the process. The resulting morphologies, a function of the liquid temperature gradient and solidification rate, are categorized by solidification modes to include planar,

5 Conclusions

A strong form-based collocation methods has been applied to discretize a multi-phase field model developed by [8] and study non-equilibrium, i.e. rapid solidification behavior for an Al-0.2 at% Sn alloy with the finite dissipation e ects. Temperatures for the dilute alloy were set between liquid and eutectic regions, at a point where the solid Al, i.e. FCC phase evolves from the mixture. Gibbs energy curves for the system were constructed from experimental parameters and methodologies given in the COST-507database [34]; note that details are described in Appendix A.

Initial analysis of two symmetrically positioned grains under periodic boundary conditions illustrated interface and chemical free energy e ects on phase and concentration field kinetics. Subsequent multi-grain solidification studies for the 10-grain and 20-grain case provided insight in the concentration profile of the fully solidified material. The results show that solid phase Al forming within grain interior with Sn solute ejected towards the boundary with highest concentrations located the intersection of multiple grain boundaries. Finally, the field equations were evaluated for alloy solidification in the presence of a 20-grain substrate. A resulting morphology exhibited a planer type solidification mode with three large grains extending from the grains sub-

Fig. 7 Discretized $10 \times 20\,\mu m^2$ computational domain of Al-0.2% Sn mixture formed by a union of solid domain, i.e. lower half and liquid domain, i.e. upper half

used to calculate free energies of pure element and multi-component systems. The coefficients are temperature T dependent and are used with the power series to evaluate the molar free energy g for a pure species i in phase γ with respect to its stable state enthalpy; i.e.

$$g_i^{\gamma}(T) - h_i^{\gamma}(\quad 8.1K) = a + bT + cT\ln T + dT \quad + eT^3 + fT^{-1} + gT^7 + hT^{-} \quad . \tag{33}$$

The free energy of multi-component system consists of contributions from each constituent species within the mixture and of mixing between species. Contributions from mixing are further classified as either ideal or non-ideal where the latter is modeled with a Redlich-Kister polynomial that contains temperature dependent interaction parameters L^{ν}. For a substitutional three-component alloy system, the free energy is given by

$$G^{\gamma}(x_i, T) = \sum_{i=1}^{3} x_i g_i^{\gamma} + RT \sum_{i=3}^{3} \sum_{j>i}^{3} x_i x_j \sum_{\nu=0}^{3} L_{ij}^{\nu}(x_i - x_j)^{\nu} + \sum_{i=1}^{3} \sum_{j>i}^{3} \sum_{k>j}^{3} x_i x_j x_k (x_i L_{ijk}^{0} + x_j L_{ijk}^{1} + x_k L_{ijk}^{2}) \tag{34}$$

where the right hand side terms respectively correspond to the unmixed, ideal mixing, binary non-ideal, and ternary

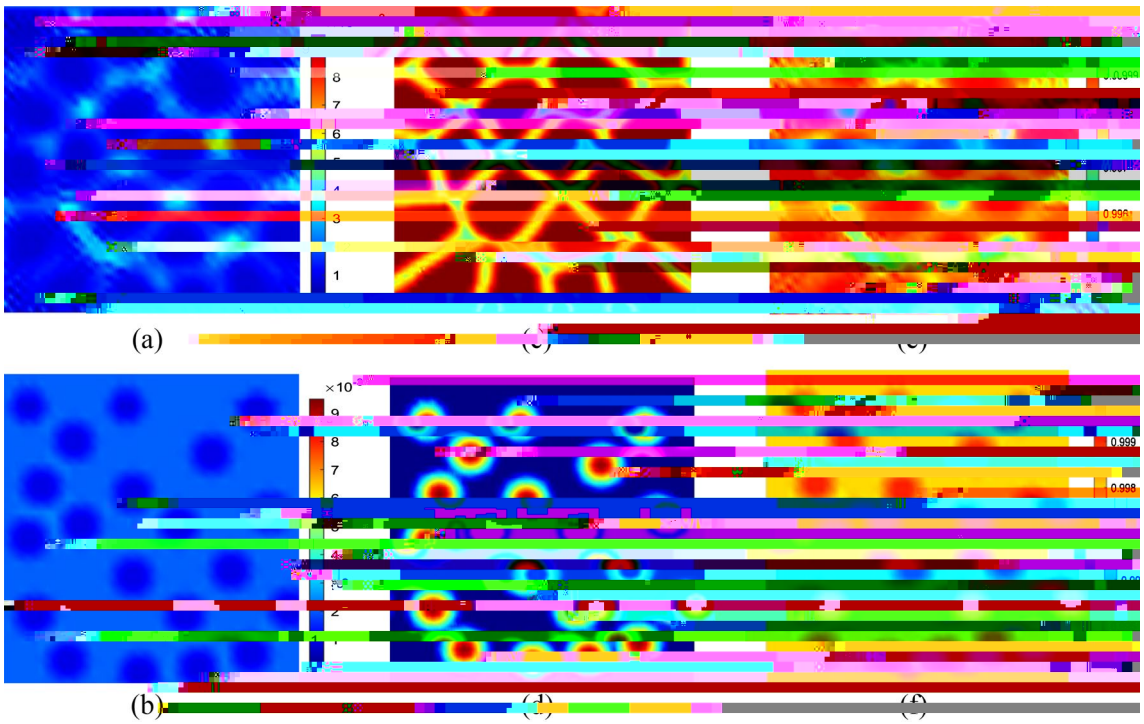

Fig. 8 Concentration and phase fields in Ω^1 for: **a** initial and **b** final Sn concentration, **c**, **d** solid phase, and **e**, **f** Al concentration

non-ideal mixing terms. Invoking the chain rule to di erentiate Eq. (34) with respect to composition yields

$$\frac{\partial G^{\gamma}(x_i, T)}{\partial x_m} = \frac{\partial G^{\gamma}(x_i, T)}{\partial x_i}\frac{\partial x_i}{\partial x_m} = G^{\gamma}_{,i} x_{i,m} \tag{35}$$

with

$$\begin{aligned}\frac{\partial G^{\gamma}(x_i, T}{\partial x_m} \quad & \sum_{i\ 1}^{3} x_{i,m} g_i^{\gamma} \quad RT \sum_{i\ 1}^{3} (x_{i,m}) \ln x_i \quad 1 \\ & \sum_{i\ 1}^{3}\sum_{j>i}^{3} (x_{i,m}x_j \quad x_{j,m}x_i \quad \sum_{\nu\ 0}^{n} L_{ij}^{\nu} (x_i - x_j)^{\nu} \\ & \sum_{i\ 1}^{3}\sum_{j>i}^{3} x_i x_j \sum_{\nu\ 0}^{n} \nu L_{ij}^{\nu} (x_i - x_j)^{\nu-1} (x_{i,m} - x_{j,m}) \\ & \sum_{i\ 1}^{3}\sum_{j>i}^{3}\sum_{k>j}^{3} (x_{i,m}x_j x_k \quad x_i x_{j,m} x_k \quad x_i x_j x_{k,m}) x_i L_{ijk}^{0}\end{aligned} \tag{36}$$

Note that for the constraint, i.e. $\sum x_i = 1$ we use the conditional relation to implement Eq. (36) in our computational analysis program:

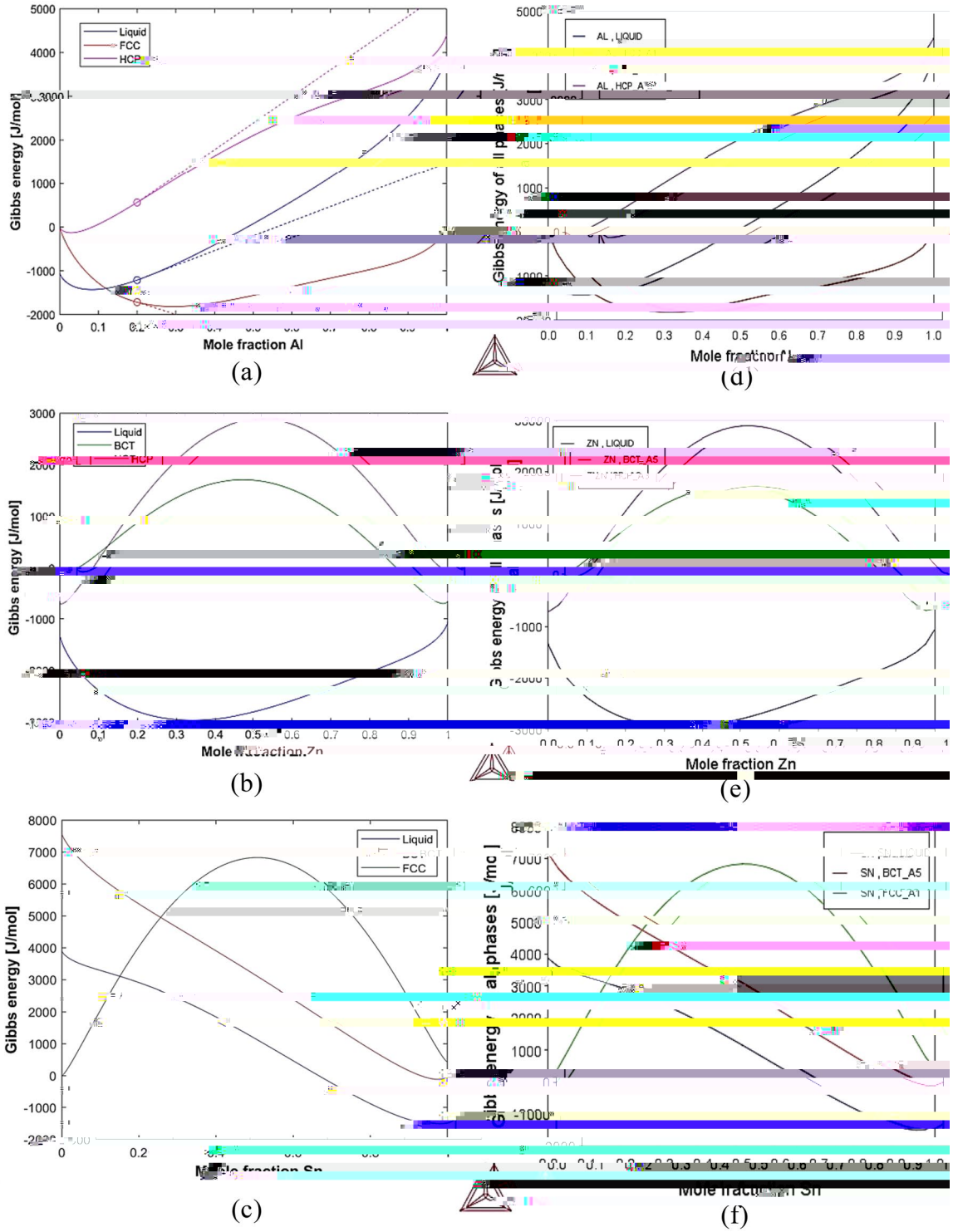

Fig. 10 Comparisons of the computed Gibbs energy (**a**–**c**) against Thermo-Calc software (**d**–**f**) at the same temperature, i.e. T **=** 600 K; the calculated Gibbs energy at along each edge of the Al–Sn–Zn ternary system, i.e. (Al, Sn, Zn = 0), (Al, Sn = 0, Zn) and (Al = 0, Sn, Zn) are shown

Note that there also exist similar properties for $\mathbb{R}^3$ domains and higher ordered derivatives (i.e $m > 2$) as well.

Another way to measure the e ectiveness of di erential operators is through its interpolation error. This may be achieved by benchmarking solution data for a given partial di erential equation against data from another known or trusted solution analytical, numerical, or manufactured solution. In this work, we take the latter approach by

manufacturing and di erentiating two primary fields $c(x, y)$ and $\phi(x, y)$ as shown in Eqs. (38) and (39) respectively to produce a term $\nabla \cdot (\phi(x, y)\nabla c(x, y))$. The manufactured fields are variants of those taken from a helpful report on the method of manufactured solutions [38].

$$(\ , \ ) = \ _0\left[1 + \sin^2\left(-\right)\sin^2\left(\frac{2}{-}\right)\right] \tag{38}$$

$$\phi(x, y) = \phi_0\left[\sqrt{x^2}\right. \tag{39}$$

Figure 11 presents a comparison between analytical y and approximate solution y^h fields for the term $\nabla(\phi(x, y)D\nabla c(x, y)$ which test all two-field first order derivative products, second order derivatives and combinations thereof; for the computation, an unit square domain is discretized with uniformly distributed 4900 collocation points. The computed discrete L_2 norm error which is given by

was measured at a value less than 0.3%. Those who interested in the computational resources to construct di erential operators are referred to Sect. 4 of this study.

8. Steinbach I, Zhang L, Plapp M (2012) Phase-field model with finite interface dissipation. Acta Mater 60(6–7):2689–2701
9. Zhang ISL (2012) Phase-field model with finite interface dissipation: extension to multi-component multi-phase alloys. Acta Mater 60(6):2702–2710
10. Reuther K, Hubig S, Steinbach I, Rettenmayr M (2019) Solute trapping in non-equilibrium solidification: a comparative model study. Materialia 6:100256
11.